Optimization of the SNR-Resolution Tradeoff for Registration of Magnetic Resonance Images

Shoan C. Kale,[1,2]* Jason P. Lerch,[1] R. Mark Henkelman,[1,2] and X. Josette Chen[1,2]

[1]*Mouse Imaging Centre, Hospital for Sick Children, Toronto, Ontario, Canada*
[2]*Department of Medical Biophysics, University of Toronto, Toronto, Ontario, Canada*

Abstract: Image registration serves many applications in medical imaging, including longitudinal studies, treatment verification, and more recently, morphometry. Registration processing is regularly applied in magnetic resonance (MR) images, where imaging is highly adaptable in capturing soft tissue contrast. To obtain the greatest registration accuracy in MR imaging, the inherent imaging tradeoff between SNR and resolution at a given scan time should be optimized for computational accuracy, rather than human viewing. We investigated this SNR-resolution tradeoff to optimize registration for digital morphometry. Tradeoff images were simulated from acquired gold standard MR images to emulate a shorter, constant acquisition time, but at the expense of SNR, resolution, or both. The group of images from each tradeoff was nonlinearly registered toward an average atlas producing deformation fields, useful for identifying differences in morphology. The gold standard data were also registered. The deformation fields were used to evaluate registration performance of each tradeoff relative to the gold standard. For fixed scan times, the optimal SNR for registration with MR imaging was found to be ~20. Image resolution should be adjusted to produce this target voxel SNR when registration is a central processing task. *Hum Brain Mapp 29:1147–1158, 2008.*

Key words: brain mapping; atlases; computer-assisted image processing; computer simulation; phenotype

INTRODUCTION

Over the last 20 years, image registration has played an increasing role in the extraction of understanding from medical images. The field is now mature, offering very sophisticated and popular treatments of nonlinear registration, including elastic- [Bajcsy and Kovačič, 1989], viscous-fluid- [Christensen et al., 1996], and set of basis functions [Friston et al., 1995] models of deformations. Today, registration facilitates many biomedical applications, including the planning and evaluation of radiotherapeutic and surgical procedures [Hill et al., 1994; Lu et al., 2006; Roeske et al., 1995], longitudinal studies [Kohn, 2002; Puri et al., 2001], and building of digital atlases [Hyunjin et al., 2003; Li et al., 2003; Toga and Thompson, 2001]. A plethora of comparative morphometric and functional studies have been carried out using automated registration techniques and analyses, such as producing probabilistic statistical atlases of cortical change in neuropathologies [Narr et al., 2005; Rüsch et al., 2003; Thompson et al., 1998, 2001], and identifying regional brain dysfunction in association with symptoms of dementia [Holthoff et al., 2005; Mega et al., 2000]. For a selected review, refer to Miller [2004].

Contract grant sponsors: Canadian Institutes of Health Research; National Cancer Institute of Canada; National Institutes of Health; Ontario Consortium for Small Animal Imaging.

*Correspondence to: Shoan Kale, Mouse Imaging Centre, Hospital for Sick Children, 555 University Avenue, Toronto, Ontario M5G 1X8. E-mail: skale@phenogenomics.ca

Received for publication 5 April 2007; Revised 17 May 2007; Accepted 25 June 2007

DOI: 10.1002/hbm.20453

Published online 23 October 2007 in Wiley InterScience (www.interscience.wiley.com).

Registration has been used extensively with magnetic resonance (MR) images, where imaging provides great versatility in capturing neuroanatomy. Data can be acquired as isotropic three-dimensional (3D) volumes or two-dimensional slices, with arbitrary resolution and orientation, while the field-of-view (FOV) can be defined to fit almost any object. The user has considerable discretion over the appearance of the resulting images, within hardware constraints and imaging time limitations. Generally, acquisition parameters are adjusted such that the images produced satisfy visual preferences. However, an imposition often overlooked is that the task of image registration is a computer analysis problem, and thus optimization of imaging parameters should respond to the needs of the computer registration.

Among the many possible optimizations one faces in MR imaging, one commonly encountered is the tradeoff between voxel size and signal-to-noise-ratio (SNR) for a given imaging time. Images with large voxels (low resolution) experience partial volume averaging of different tissues at boundaries, which blurs details in images, but can benefit from relatively high SNR and thus contrast. For the same acquisition time, images with small voxels (high resolution) can also be produced, but their low SNRs obscure details in low contrast regions of the image. In MR, this tradeoff between resolution and SNR is real, unlike instances in ionizing radiation imaging modalities where the tradeoff between resolution and SNR is apparent [Constable and Henkelman, 1991; Edelstein et al., 1986; Fuderer, 1988]. This apparent tradeoff in ionizing radiation imaging modalities comes from the fact that the noise in any pixel is photon-limited and hence proportional to the square root of the signal. Therefore, SNR in a finely sampled X-ray CT image can be recovered to that of a coarsely sampled image through rebinning of neighboring pixels. This compensation for SNR through rebinning cannot be achieved in MR in which noise is independent of the signal, and at fixed scan times, increasing resolution leads to an irrecoverable loss in SNR. This peculiarity to MR imaging is well known among its users: An image acquired at a particular SNR-resolution combination cannot be processed to recover a different SNR-resolution combination for the image acquired at the same imaging time. Thus, image-processing algorithms that attempt to recover SNR through the standard Gaussian blurring method will not recover the full SNR of the image acquired, from the outset, with the same final resolution for the same imaging time. Furthermore, the choice of SNR-resolution tradeoff is important, because at a given image contrast, defined by tissues' T_1 and T_2 values, the chosen pulse sequence, the application of contrast agent, etc., it is SNR and resolution that have the most profound effects on image quality [Owen and Wehrli, 1990]. Accordingly, the MR user must make a decision as to how to allocate scan time between increasing SNR or improving resolution for a given imaging time to acquire the most appropriate image.

Recognizing that the problem of registration is a computer analysis task and not a human vision task, we investigate the optimization of the tradeoff between SNR and resolution in MR imaging for constant scan time, such that optimal registration accuracy is achieved. Such knowledge is valuable for streamlining studies of computational anatomy for improved reliability and statistical power. The approach chosen involved simulation of tradeoff images from a gold standard group of images, independently registering each group toward an unbiased average atlas, and evaluating the accuracy of the registrations by directly comparing the resulting deformation fields against those of the gold standard group.

METHODS AND MATERIALS

We make the basic assumption that MR imaging of different anatomies contain a sufficient variety of structures and contrasts that an optimization based on registration performance should be independent of the choice of anatomy. However, specialized imaging, such as MR angiography, would be inappropriate as representative of general anatomical images. We approached this optimization problem using images of fixed mouse neuroanatomy acquired through a high quality microscopy protocol developed at the Mouse Imaging Centre, Toronto.

Tissue Preparation

Brain specimens, imaged in situ, were prepared similar to methods described previously [Henkelman et al., 2006; Tyszka et al., 2006]. Briefly, 10 genetically identical male and female C57BL/6 wild-type mice, ~6 weeks of age, were anesthetized using a mixture of xylazine (Rompun®, Bayer Animal Health, Toronto, ON, Canada) (20 mg/kg) and ketamine (Rogarsetic®, Pfizer Animal Health, Kirkland, QC, Canada) (100 mg/kg). The animals were then perfused (30 ml phosphate buffered solution (PBS)) and fixed (30 ml of iced 4% paraformaldehyde (PFA)) prior to decapitation, where the skin, lower jaw, ears, nose tip, and zygomatic bones were removed from the head. The remaining skull-brain structures were placed in a bath of 4% PFA for 4–5 h at 4°C, and then transferred to a solution containing PBS and 0.01% sodium azide for 7 days on a nutator. The brains were then transferred into a similar solution, including a 2 mM concentration of Prohance© (Bracco Diagnostics Canada, Mississauga, ON, Canada) and nutated for at least 7 days to allow diffusion of the contrast agent through the skull. Immediately prior to imaging, brains were blotted and immersed in Fluorinert© (3M Specialty Materials, St. Paul, MN) within a plastic tube. All animal protocols were approved by the Hospital for Sick Children Animal Care Committee.

Imaging Protocol

All imaging was completed on a 7-T superconducting magnet (Magnex Scientific, Oxford, UK) with a multichannel Varian^{INOVA} console (Varian NMR Instruments, Palo Alto, CA) and a three-coil probe for parallel sample imaging [Henkelman et al., 2006]. The mean values of T_1 and T_2 in brain parenchyma were measured to be 175 ± 16 and 28 ± 2 ms. A fast spin-echo (FSE) pulse sequence was used (TR/TE = 325/8 ms) with six echoes (the center of *k*-space acquired on the fourth echo, TE_{eff} = 32 ms), 90° flip angle, 14 mm × 14 mm × 25 mm FOV, an acquisition matrix of 432 × 432 × 780, and four signal averages (NA). The total imaging time was 11.3 h, and yielded T_2-weighted images of three brains per scan session with 32-μm isotropic voxels. A total of 10 brain samples were scanned. Image reconstruction for 10 scanned samples was performed on a 2-GHz dual-processor, 64-bit Linux workstation with 8-GB RAM, using Matlab R13 (MathWorks, Natick, MA) computational software. The mean SNR of the reconstructed magnitude images, in homogeneous gray matter regions of the brain, was 16. These data represented the gold standard group of images.

Simulation of Tradeoff Data

By simulating instead of acquiring tradeoff data, we effectively recreated identical imaging conditions for the images in each of the tradeoff groups. For example, all tradeoff data would share exactly the same artifacts, shimming, gradient behavior, temperature fluctions, etc., that could otherwise potentially vary over separate scans. Therefore, the deviations in registration introduced by such variations can be eliminated. Furthermore, simulating images allowed a great degree of control to be exercised over the choice of fixed imaging time to produce tradeoff data retrospectively. It was important to produce tradeoff data that covered a sufficiently wide range of SNRs and resolutions, while providing images of reasonable overall image quality.

Using this strategy, resolution and SNR tradeoff data were simulated for a sixfold shorter, fixed imaging time by degrading each of the gold standard data through a two-step process. The procedure is described for one gold standard image.

The first step involved selecting subvolumes from the center of gold standard *k*-space data to produce increasing voxel size (reduced resolutions) among reconstructed images. This corresponded to reduced effective acquisition times as phase encode dimensions were decreased. Subvolumes were chosen to give a factor of 2 in voxel volume between five consecutive tradeoff images, yielding isotropic resolutions of 32, 40, 51, 64, and 81 μm, hereafter referred to as tradeoffs *A*, *B*, *C*, *D*, and *E*. The second step simulated adjusting the total effective imaging time among the different volumes of *k*-space data. Denoising of images to emulate increased signal averaging cannot be effectively implemented, because all noise removal strategies [Bao and Zhang, 2003; Sijbers et al., 1998] compromise resolution through blurring or bias the intensity distribution nonuniformly in the magnitude images [Ghugre et al., 2003]. Instead, reduced signal averaging and a corresponding reduced fixed imaging time (1.8 h) was simulated by adding zero-mean, Gaussian-distributed white noise [Nishimura, 1996] to the measured raw data. The particular amount of noise added to each tradeoff volume was determined as follows. The relative NA for each *k*-space tradeoff volume was calculated as the total number of phase-encoding steps of the largest tradeoff volume over the total number of phase-encoding steps of each tradeoff volume (Table I). Since each NA reduces the standard deviation of noise in *k*-space by $\sqrt{\mathrm{NA}}$, the target standard deviation of noise for *k*-space tradeoff *i*, $i = A, B, C, D, E$, was determined as

$$\sigma^i_{\mathrm{tar}} = \sigma_k \sqrt{\frac{\mathrm{NA}^E}{\mathrm{NA}^i}}. \quad (1)$$

Here, σ_k is the initial standard deviation of noise for the real and imaginary channels of each data acquisition, and was ascertained from the mean of the standard deviations of noise in a signal- and artifact-free region of real and imaginary image space [Henkelman, 1985]. Note that σ^i_{tar} decreases with *k*-space volume and $\sigma^i_{\mathrm{tar}} = \sigma_k$ for tradeoff *E*.

TABLE I. Tradeoff images simulated for 1.8-h scan time[a]

Tradeoff	Voxel volume (10^3 mm^3)	*k*-Space samples ($PE_1 \times PE_2 \times RO$)	Isotropic resolution[b] (μm)	Relative NA[c]	Mean SNR[d]
A	0.033	432 × 432 × 780	32	1.0	6.4
B	0.066	344 × 344 × 620	40	1.6	11.3
C	0.131	272 × 272 × 492	51	2.5	20.2
D	0.262	216 × 216 × 390	64	4.0	35.9
E	0.524	172 × 172 × 310	81	6.3	63.0

[a] Information for the first set of images simulated from the acquired gold standard data by trading up resolution and/or signal averaging (SNR) for a constant effective imaging time of 1.8 h.
[b] The isotropic resolution factor between tradeoff images is $\sqrt[3]{2} \approx 1.26$.
[c] The relative NA between tradeoffs is $\left(\sqrt[3]{2}\right)^2 \approx 1.59$.
[d] The SNR factor between tradeoffs is $\left(\sqrt[3]{2}\right)^{5/2} \approx 1.78$.

Finally, since variances add, the standard deviation of zero-mean, Gaussian-distributed noise, σ_u^i, added independently to the real and imaginary parts of *k*-space tradeoff data *i* was

$$\sigma_u^i = \sqrt{{\sigma_{\text{tar}}^i}^2 - \sigma_k^2}. \quad (2)$$

Random numbers for noise were generated using the normal-distribution random number generator in Matlab R13, which samples from the entire normal distribution with a period much greater than the number of samples generated. Tradeoff images were produced by this method for each of the gold standard brain images acquired from the 10 mice. The mean SNR in a homogeneous white matter region of the brain is reported in Table I for the tradeoffs produced.

Registration of Images

Image registration was executed through a semiautomated processing pipeline set up and used regularly at our facility. All processing applied the intensity-based ANIMAL methodology (Brain Imaging Centre, McGill University, Montreal) [Collins and Evans, 1997; Collins et al., 1994, 1995]. ANIMAL is a nonlinear, mesh-warping registration algorithm, offering a multiscale, multiresolution hierarchy to registration, for increased efficiency and accuracy. The algorithm functions on a nested loop—the outer loop manages the resolution scale at which registration operates and the inner loop optimizes the similarity metric between the source and target images. The inner loop is parameterized by the chosen similarity metric, a mesh-stiffness parameter, and a weighting parameter, to either under- or overcorrect displacements between iterations.

Mesh-warping algorithms work well for the modeling brain deformations. While other methods should produce similar results, ANIMAL has been shown previously to be useful in the neuroanatomical registration of various strains of mice [Lerch et al., 2006; Spring et al., 2007]. For this reasons, and because of local expertise in its implementation, the ANIMAL algorithm was chosen. The particular implementation has been described in more detail previously [Kovacevic et al., 2005; Lerch et al., 2006] and is summarized later for one tradeoff group of 10 images.

Initially, the native images were aligned to a model brain in a standard orientation using rigid-body registration to remove gross positional differences. The FOVs were cropped to match that of the model brain image and then images were intensity-corrected using the nonparametric nonuniform intensity normalization (N3) algorithm [Sled et al., 1998]. Next, each brain was spatially transformed with an average affine transformation, generated by performing affine registration with every other brain in the group and finding the mean. Then the affinely registered brains were averaged together to produce a new target model atlas. This coregistration and averaging of brains eliminate bias when constructing the brain atlas [Kovacevic et al., 2005]. Subsequently, brains were nonlinearly registered toward a target atlas using a hierarchical, multiscale, multiresolution approach over six to seven iterations, the target at each iteration being updated from the average of registered brains in the preceding iteration. The nonlinear registration method used a deformable elastic model, thereby producing deformation vector fields to map source to target, with grid spacing down to the natural resolution of the native files. The similarity measure used in all registration steps was the normalized cross-correlation metric [Collins et al., 1994]. All source and target images were smoothed before registration, by convolving images with Gaussian blurring kernels with full widths at half maximum ranging from 2.5 mm in the rigid-body registration to 60 μm in the nonlinear registration.

Registration was completed on the gold standard group of images and each of the tradeoff groups independently.

The registration algorithm was particularly sensitive to large amounts of noise in the images. This point has been noted previously by others [Collins et al., 1995; Holden et al., 2000; Lemieux and Barker, 1998]. In particular, images in tradeoff groups *A* and *B*, with mean SNRs of 6.4 ± 0.5 and 11.3 ± 1.0 were the most difficult to automatically register, even at the stage where rigid-body registration was used to roughly orient native images into a standard space. In these cases, an additional image blurring step was necessary to ensure convergence to a solution in the rigid-body registration step. Following the successful convergence of these rigid registrations, the temporary images were discarded, and the recovered transformations were applied to the native images before proceeding to the affine registration step.

Evaluation of Registration

Performance of registration for each tradeoff group *i*, relative to the gold standard registration, was evaluated by computing the root mean square error (RMSE) metric [Collins and Evans, 1997; Collins et al., 1995; Freeborough et al., 1996; Holden et al., 2000; Lemieux and Barker, 1998],

$$\text{RMSE}^i = \sqrt{\frac{1}{N}\sum_{n=1}^{N}\left\|\mathbf{d}^o(\mathbf{r}_n) - \mathbf{d}^i(\mathbf{r}_n)\right\|^2} \quad (3)$$

of the deformation fields mapping nonlinear atlases back to the affine space, where $\mathbf{d}^o(\mathbf{r}_n) - \mathbf{d}^i(\mathbf{r}_n)$ is the *n*th error vector found by a direct vector subtraction of the tradeoff image *i* deformation vector from the gold standard deformation vector *o* at location **r**. *N* is the number of voxels in the brain. Note that the gold standard deformation fields were transformed into the final nonlinear space of the tradeoff groups and all deformation fields were resampled to 32 μm using sinc interpolation before vector subtraction.

TABLE II. Tradeoff images simulated for 4.5-h scan time[a]

Tradeoff	Voxel volume (10^3 mm^3)	*k*-Space samples ($PE_1 \times PE_2 \times RO$)	Isotropic resolution[b] (μm)	Relative NA[c]	Mean SNR[d]
F	0.033	432 × 432 × 780	32	1.0	10.0
G	0.066	344 × 344 × 620	40	1.6	18.3
H	0.131	272 × 272 × 492	51	2.5	32.9

[a] Details on resolutions and SNRs for the second set of images generated for an effective imaging time of 4.5 h, the geometric midpoint between the acquisition times of the gold standard and 1.8-h time-point data.
[b–d] (Same as Table I).

The gold standard deformation fields were mapped into the corresponding nonlinear space of each of the tradeoff groups individually. For example, for the gold standard deformation field of one brain, this was achieved by mapping the field back to the original native space, common to all groups, then mapping it forward to the final nonlinear (atlas) space of the corresponding tradeoff group. The transformations used to map the gold standard deformation field back to the native space included the inverse nonlinear and inverse affine gold standard transformations, and those used to map the field forward to the nonlinear space of the corresponding tradeoff group included the forward affine and nonlinear transformations.

To ensure that the final evaluation of the optimum registration accuracy was not an artifact of the particular choice of imaging time, the complete experiment was repeated for an intermediate fixed imaging time. Three tradeoff groups, referred to as *F*, *G*, and *H*, were simulated for a 4.5 h imaging time. Details for these data are outlined in Table II.

RESULTS

An example of the gold standard data is shown in Figure 1 (left panel) as coronal and horizontal slices of one brain. The images are isotropic with high resolution and SNR. At the center, a selected view of the anterior commissure, from the horizontal slice, is shown where the high contrast and image quality is appreciable. To visualize the differences among the produced tradeoff images and the gold standard image, the anterior commissure from the corresponding tradeoff images *A–E* are displayed in the column of images on the right-hand panel. Note that while tradeoff *A* (top of column) still has high resolution there is a definite loss of contrast because of high levels of noise. Conversely, tradeoff *E* (bottom of column) loses resolvability from increased partial volume effects of larger voxels while the SNR remains high. The transitional tradeoff images, *B* to *D*, show intermediate levels of contrast and partial volume effects. The measured SNRs of the simulated tradeoff images were within 1% of the targeted SNRs.

Registration succeeded in converging to an average atlas for all groups of images. The registration process is illustrated for the gold standard group of images in Figure 2, which shows representative coronal slices of input brains following rigid-body registration, the average atlas of affinely registered brains, and the final nonlinear average. One can appreciate the value of removing biological variability through nonlinear registration by comparing the affine and nonlinear averages. For example, the arrowheads emphasize two areas where anatomy can be readily identified in the nonlinear atlas, whereas the incongruency of affinely registered brains make these anatomies unresolvable in the affine average. It should be noted in this figure that the main outputs of the nonlinear registrations are deformation fields, a 3D vector displacement map for each input image, which encode local spatial mappings from affine to nonlinear space. It is the accuracy of these deformation fields that are evaluated against the gold standard.

To visualize the comparison of deformations among tradeoff and gold standard deformation fields, an example is illustrated in Figure 3 for the registration of one brain from the group of 10 brains. The leftmost image shows a reference coronal slice from the associated gold standard brain where two points are sampled to make voxelwise comparisons in the corresponding tradeoff and gold standard deformation fields. The sampled points were chosen retrospectively to test the behavior of displacement vectors: one point was chosen in a region where the errors in deformation relative to the gold standard were found to be relatively small (pink circle, mean displacement error ± SD = 46 ± 12 μm) and another point where the errors were large (blue circle, 159 ± 28 μm). Computer-rendered 3D images of the inverse displacement vectors from the tradeoff and gold standard deformation fields are shown at the middle of the figure for these two sampled points. The vectors verify that deformations are similar among all SNR/resolution tradeoff and gold standard groups, yet small deviations of tradeoff vectors are visible relative to the gold standard vectors. Vector subtraction of tradeoff displacement vectors from the gold standard displacement vectors produces vectors of displacement error relative to the gold standard. This is repeated for all points in the brain. The magnitudes of the resulting displacement error vectors (ME), equivalent to $\|\mathbf{d}^o(\mathbf{r}_n) - \mathbf{d}^i(\mathbf{r}_n)\|$ in Eq. (3), are presented as maps on the right for the corresponding tradeoff coronal slices, with the two sampled points indicated. The regional distributions of error are common across tradeoffs. The brighter intensities at the point where

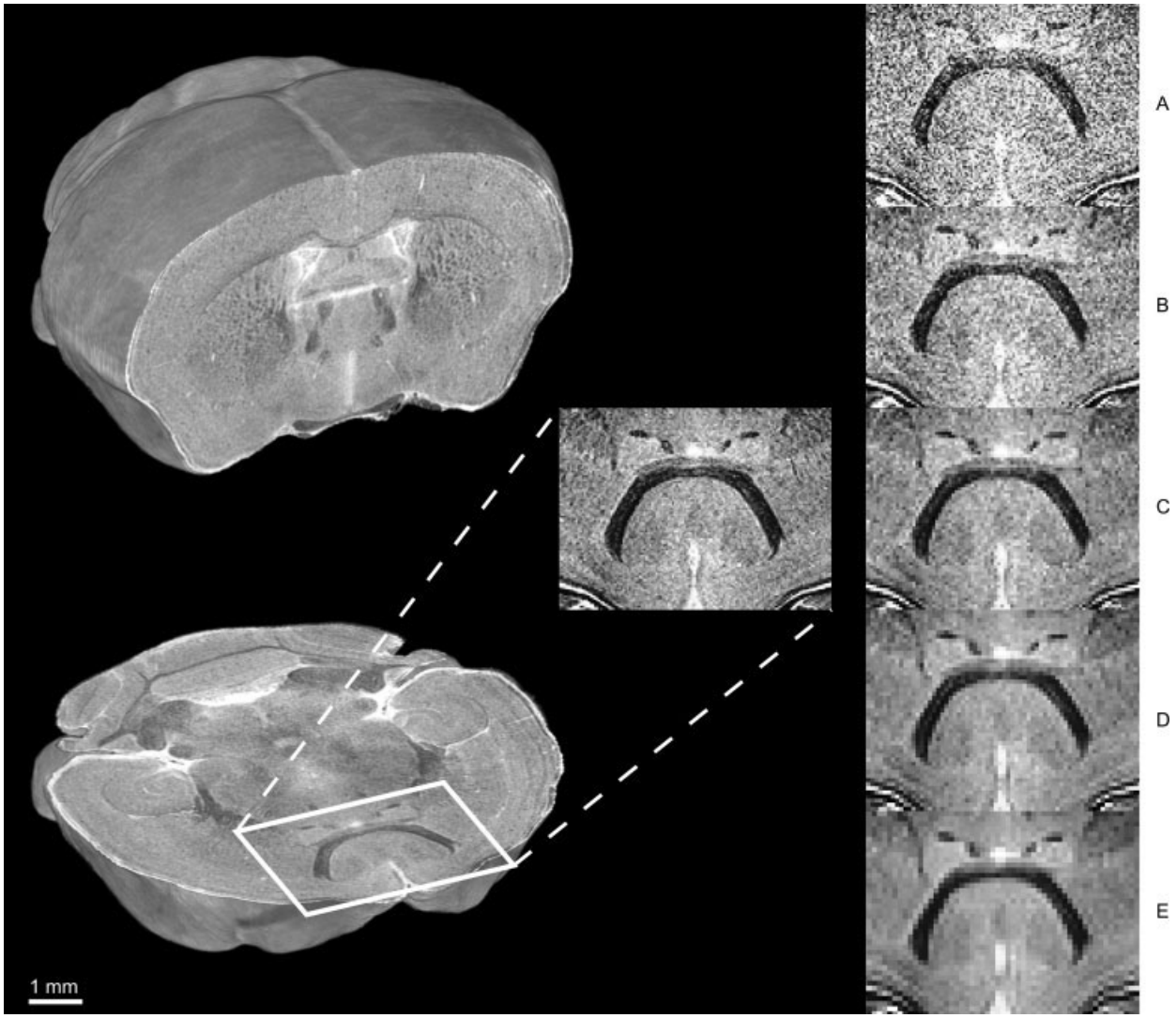

Figure 1.

The acquired gold standard and simulated tradeoff data for an effective imaging time of 1.8 h. Coronal and horizontal profiles from a single volume-rendered brain of the gold standard group are shown in the panel on the left, illustrating the high resolution and SNR of these acquired images; a selected view of the anterior commissure from the horizontal profile is shown at the center. The panel on the right shows the anterior commissure of the corresponding brain in tradeoff groups **A**–**E** for comparison.

the triangles reside (cortex) represent larger displacement errors, which contrasts with the hypointensities at the point where the circles reside (subcortical region where contrasts are greater) which represent lower displacement errors. It can already be seen that errors appear least in *C*.

To determine the RMSE registration value across the whole brain, the deformation fields for tradeoff images representing the 1.8-h time point were evaluated against the gold standard using Eq. (3). For the chosen brain in Figure 3, the RMSE in deformations for each tradeoff is organized into the log–log plot shown at the top left of Figure 4. Similar plots are displayed below this, corresponding to registration accuracy among tradeoffs for the other nine brains. The minimum error in each curve is found consistently for tradeoff *C*, except in only one case. Compiling this information into a single curve, Figure 5 shows a log–log plot of mean RMSE versus mean SNR (•) across the 10 brains, with error bars given as standard error of the mean (SEM). There is a clear minimum to the curve occurring at tradeoff *C*, corresponding to an SNR of ~20. To verify that the optimal tradeoff reflects SNR only and was independent of total imaging time, another set of tradeoff images was produced at larger constant imaging time (refer to Table II), registered toward nonlinear atlases, and evaluated. Results for the evaluation of registration performance of these 4.5-h time-point images are also

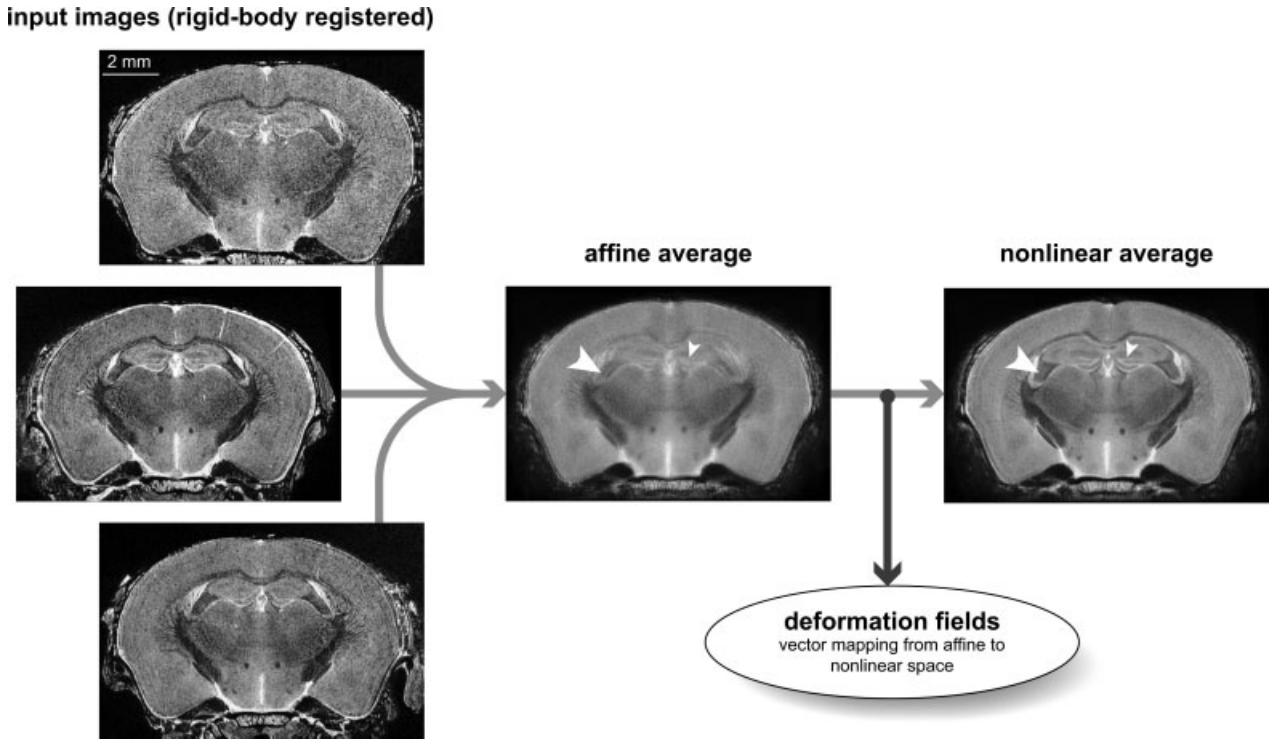

Figure 2.

Basic diagram outlining the major steps in coregistering brains toward an average brain. The input images here (subset shown) have previously been registered to a mouse brain in a standard orientation using rigid-body registration. Each brain is affinely registered to the other input brains to determine an average affine transformation. The volumes are then resampled using these average affine transformations. A coronal slice of the average of affinely registered brains is shown in the center. Subsequently, multiscale elastic deformations are applied to each brain to bring them into a common nonlinear atlas space (described in Methods). The corresponding slice of the nonlinear average is shown at the right. Note that the deformation fields needed for evaluation of registration accuracy are created in the process of nonlinear registration. Two features are highlighted in the averages which show significant improvement following nonlinear alignment, including the dentate gyrus (small arrowheads) and the outline of the fimbria (large arrowheads).

shown in Figure 5 (×), with the minimum at tradeoff *G* still in the vicinity of an SNR of 20, which supports the assertion that the optimal SNR is invariant.

Registration accuracy was based on the evaluation of the deformation fields recovered from nonlinear registration, and thus strictly included only the nonlinear components of registration. However, nonrigid linear components of registration are also important to the assessment of biological variability. Nonrigid linear components are the space-deforming linear components of affine transformations, including three scales and three shears in orthogonal directions, which reflect important differences in volume and gross shape between source and target objects. To test all nonrigid transformations, the scale and shear portions of the average affine transformations produced during registration were incorporated into the deformation fields, and the deformation fields were evaluated as before. It was found that the mean RMSE was increased for each tradeoff case, likely because there are more independent components contributing to registration error, while the minimum still clearly occurred at tradeoff *C*, with SNR ~20 (data not shown).

As the ME maps and the RMSE metric discard directional information, the concern could arise that the orientation of the deformation vectors at corresponding locations across tradeoffs may be erratic or poorly correlated to the gold standard deformation vectors. The vectors plotted in Figure 3 demonstrate that the deformations at a given point are in a common direction among all tradeoffs relative to the gold standard for both the cases of large and small deformations. To further illustrate that the deformations are similar across brains of the gold standard and the tradeoffs even at the voxel level, we consider the angle of deviation between the gold standard and tradeoff deformation vectors for all points inside of the brains. The mean deviation angle, θ, was calculated for each tradeoff group in the 1.8-h time-point set of deformation fields relative to the gold standard, and the results are compiled in Figure 6 with error given as SEM. Deviation angles greater than or equal to 90° would create suspicion regarding the nature of the deformations,

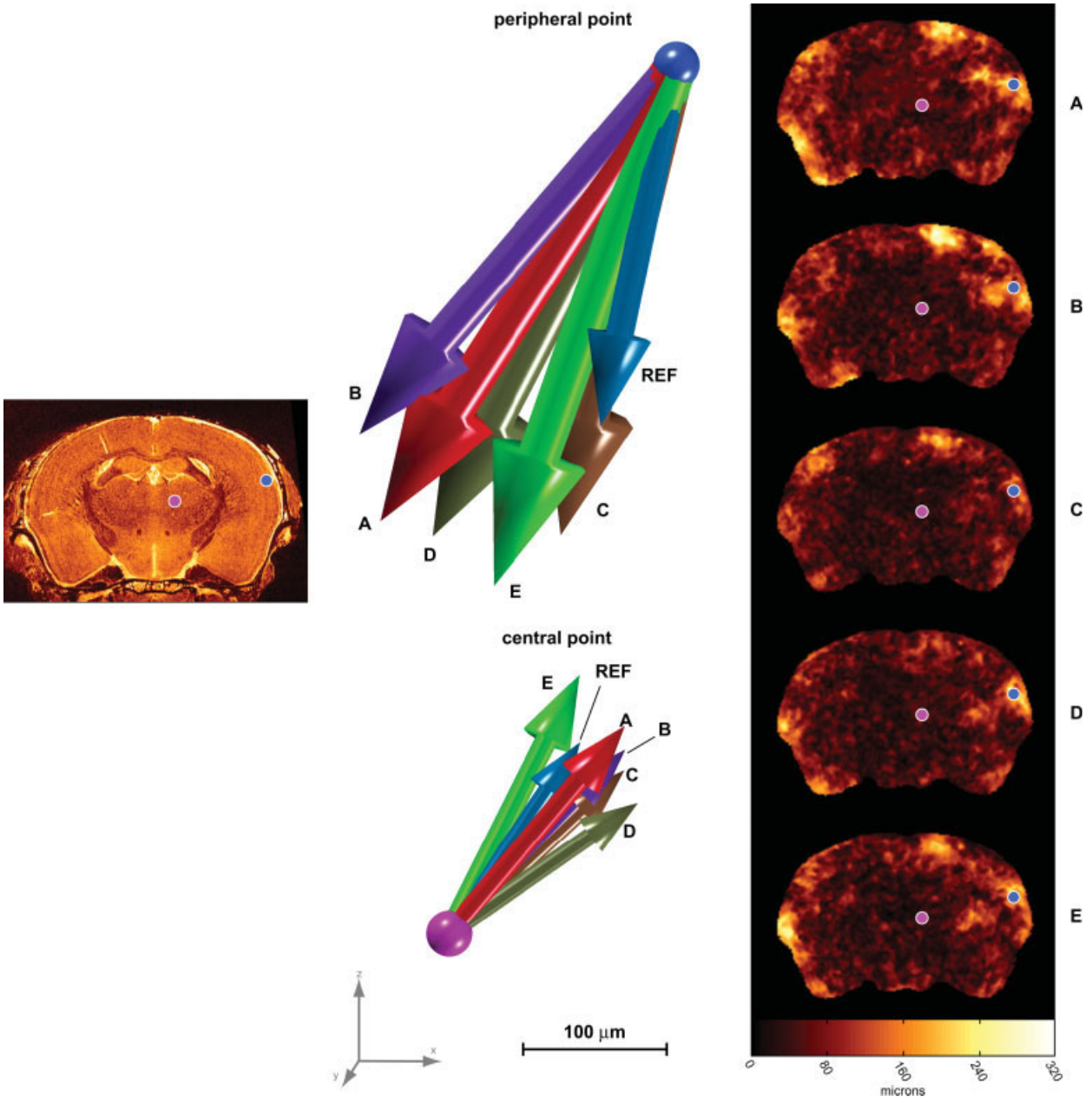

Figure 3.

A visual illustration of the error in the deformation fields relative to the gold standard in one brain. Two points (indicated by the blue and pink circles in the image on the left) are sampled from the corresponding gold standard and tradeoff deformation fields obtained from the nonlinear registrations of one brain. The individual 3D displacement vectors from the sampled points for the tradeoffs (labeled "**A**" to "**E**") and the gold standard (labeled "**REF**") are shown in the middle. Maps of the magnitude of displacement error (ME) for each tradeoff are seen at the right for the associated coronal slices, with the two sampled points highlighted in each map.

such as negative or no correlation; however, it is clear that the mean deviation angles of all tradeoffs lie wholly within 45°. It is also satisfying to see that the trend followed by the tradeoff groups is similar to that in the RMSE vs. SNR curves in Figure 5, such that the minimum mean deviation angle occurs near tradeoff *C*.

DISCUSSION

It is important to note that spatial resolution was treated as the voxel size; however, this is not strictly correct. In MR imaging, one potential resolution-degrading factor is image blurring, which is determined by the rate of expo-

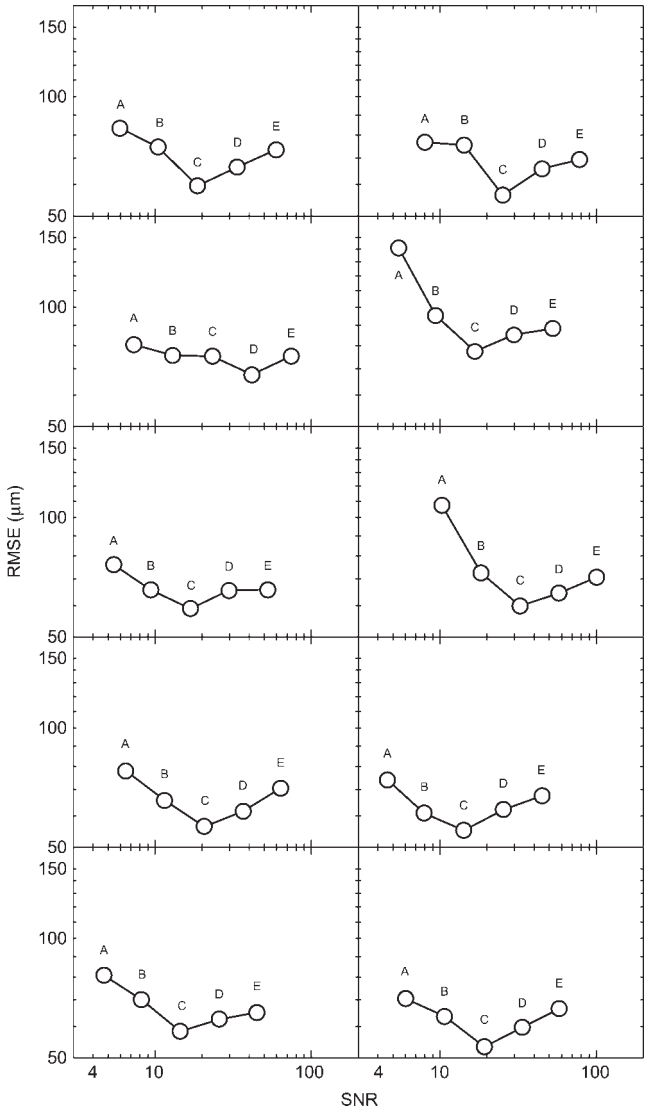

Figure 4.

Comparison of tradeoff registration accuracy relative to the gold standard for each of the 10 brains used in this study presented as plots of RMSE vs. SNR. RMSE values are calculated as in Eq. (3). The curve at the top left shows the evaluation of registration accuracy among tradeoffs for the brain chosen in Figure 3.

nential decay of the transverse magnetization, governed by T_2^* relaxation in the readout direction, during signal acquisition. Shorter T_2^* implies a greater degree of intravoxel spin dephasing due to B_0 magnetic inhomogeneities, susceptibility effects and spin–spin interactions (T_2). This means that the width of the NMR spectrum will be broader across the object, and that the true frequency-encoding of spins is offset from the expected values, leading to slight blurring in the reconstructed image in the readout direction. (A broader NMR spectrum effectively corresponds to a wider point spread function with which the image is convolved.) Additionally, in this article, a FSE pulse sequence was used, whereby the acquisition of multiple refocused echoes in *k*-space modulates the amplitude of the data in the first phase-encoding (echo train) direction. The modulation of each echo is a function of T_2 relaxation and the time at which each echo is recorded. The result is that the image is convolved with a point spread function of nonzero width in the echo train direction. According to Constable and Gore [1992], T_2 modulation, and therefore image blurring, can be minimized in the echo train direction by prescribing TE_{eff} to be a mid-to-late echo, keeping the echo train length within eight echoes, and keeping TE short. These guidelines were followed in the pulse sequence protocol, such that most of the predicted voxel resolution was recovered.

While registration accuracy of tradeoffs was measured against the registration of gold standard data, it is important to note that this registration itself represents only a best estimate of the ideal registration. For various reasons, including the fact that (1) neighboring voxels representing different biological structures often have the same or similar intensities; (2) homogeneous regions make voxelwise correspondence impossible; (3) partial volume effects can blur the signal from biologically distinct tissues, and (4) the true signal is distorted by imaging noise, a perfect registration cannot be achieved [Crum et al., 2003; Maintz and Viergever, 1998]. The FSE imaging protocol employed

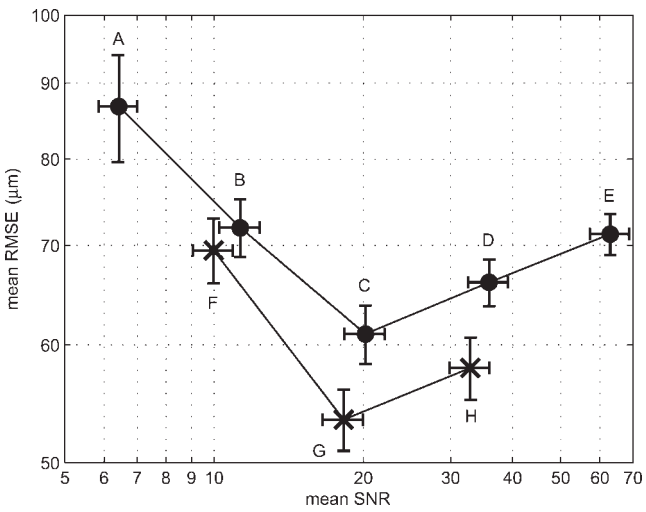

Figure 5.

Results of the evaluation of registration for the generated tradeoff images relative to the gold standard images, plotted as mean RMSE versus mean SNR on log scales. The minimum mean RMSE occurs at tradeoff *C* for data generated at the 1.8-h time-point (●), and at tradeoff *G* for data generated at the 4.5-h time-point (×), both near an SNR of 20. Error bars are given as the standard error of the mean (SEM) across the 10 brains from each tradeoff group.

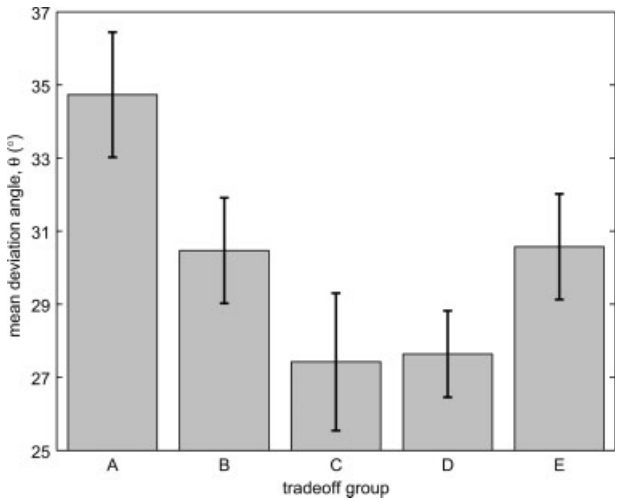

Figure 6.

Graph illustrating the mean deviation angle θ of tradeoff deformation vectors (from tradeoffs representing the 1.8-h timepoint) measured from the gold standard deformation vectors in the deformation fields. The mean angles are well below 90° and the minimum deviation angle θ occurs near tradeoff group *C*, the same group where minimum mean RMSE was calculated. Error bars are given as SEM.

was optimized to satisfy human visual preferences and tried to remove potential registration errors caused by either of the latter two points.

Given that registration accuracy of tradeoff groups was assessed relative to the gold standard using the deformation fields generated during nonlinear registration, it is important to understand their comparative behavior among tradeoffs in the brains. It is expected that larger registration errors would be shared across tradeoffs in regions of low contrast and fine details, where correspondence has a reduced probability of being established, and smaller errors to occur in regions of high contrast. In general, this is what is observed when considering the ME maps, an example of which is shown in Figure 3 (right) for a set of tradeoff images of one brain. The magnitude and distribution of errors is noticeably higher for tradeoffs *A* and *E* when compared to *C* or *D*. Note that the largest errors appear in the region of the homogeneous cortex where the expectation of determining strong correspondence is low, while the error in the center of the brain is low, given the tendency for there to be more high contrast structure at the center of the brain. Alternatively, larger errors may present in the cortex as a consequence of minor linear misregistrations during the rigid-body or affine alignment. During linear registration, the objective function may reach a maximum when the brain tissue inside of the cortex is optimally registered, since this volume of material is a considerable proportion of the whole brain and the contrasts are stronger. This, in turn, may leave the cortex slightly more misaligned in different tradeoff groups, which is then rectified by the nonlinear registration.

The determination of the optimal SNR-resolution tradeoff was made, given a specific imaging protocol including a 7-T magnet, T_2-weighted image contrast, an FSE pulse sequence, and mouse neuroanatomy. However, the result reported in this paper is expected to be generally applicable, independent of specific imaging system, pulse sequence, and anatomy. If the image-specific parameters were changed, all hypothetical tradeoff images would be affected equally in terms of the change in contrast, SNR, and even artifacts. This fact is supported by recognizing that tradeoff images could be produced from any gold standard image. As such, the relative registration performances would be expected to remain unchanged. Further, we believe that the results should be applicable to other cases of anatomical imaging, including human imaging, because the mouse brain images contained a range of contrasts at varying spatial scales that can be said to fairly represent anatomical images in general. In fact, the power spectral density of MR images, i.e., the squared magnitude of *k*-space, has been shown to possess a $\|\mathbf{k}\|^{-\alpha}$ characteristic, with $\alpha \approx 3$, in both humans (head, spine, cardiac, and knee) [Fuderer, 1988] and mice (body) [Behin et al., 2005]. This is a general observation among natural scene and fractal images: that $\|\mathbf{k}\|^{-\alpha}$ spatial statistics are scale-invariant [Field, 1987]. While not conclusive proof, the implication of this similarity is that data available in human versus mouse anatomical MR images are comparable. While the appearance of the anatomy of different organs, or even the same anatomy among different species, may be perceived as strikingly dissimilar the statistical content of the images must be similar. The treatment of such natural scene images by computer registration, must consequently be similar. As such, we believe these results are applicable to the optimization of human MR imaging for registration analysis, and should be applicable regardless of the imaging acquisition one uses or the anatomy in which one is interested.

The calculated mean RMSEs provide a means to compare the relative accuracy for each tradeoff case, but indicate little about the significance of the magnitude of these errors. The error values can be put into perspective when considering the standard deviation of deformation magnitudes (SDDM) for atlas creation introduced by Kovacevic et al. [2005]. This measure represents the biological variability among the brains of genetically identical individuals. For the gold standard group in this study, the mean SDDM over the brain is 103 μm, which is equivalent to the determined SDDM of 102 μm, also found for C57BL/6 wild-type mice in two larger studies of 20 mice, by Spring et al. [2007]. From Figure 5 it can be seen that the mean RMSE for all tradeoffs is <90 μm, suggesting that the errors are much less than the displacements themselves.

The optimization of the SNR-resolution tradeoff for registration was done using an intensity-based registration method. While intensity-based methods are more often

applied for the registration of medical images [Maintz and Viergever, 1998; Zitová and Flusser, 2003], feature-based methods are also used. Here, following the identification of a set of corresponding markers in the source and target images, registration can ensue without the influence of image voxel values. Thus, registration based on features will neither be affected by the level of noise nor by partial volume averaging of the images, because intensity-based similarity measures are not evaluated in the objective function, and the results of the SNR-resolution tradeoff for registration found in this investigation may not apply to these cases. However, the preliminary identification of corresponding markers will be affected by the SNR-resolution combination in the images. Therefore, when automated, this effectively becomes an optimization for computer feature detection rather than registration. Noisy and low-resolution images will limit the accuracy of corresponding marker identification. Investigators interested in implementing feature-based methods may need to perform a reoptimization of fixed-time tradeoff between SNR and resolution for their specific needs.

A potential limitation of this investigation is the use of one registration algorithm for the determination of the optimal tradeoff for registration. Different registration packages can implement a range of different objective functions, transformation models, and search algorithms. While it is expected that the overall performance of other registration algorithms would vary, we expect that the relative performance of these other algorithms would still yield the same relative performance in the registration of images in tradeoff groups.

It should be noted that 3D images were used in this investigation and that the results found are applicable for the registration of 3D images. Given the unavoidable presence of noise and partial volume effects in MR images, it is conceivably simpler for computer registration algorithms to establish correspondence between structures in 3D images where the data from adjacent slices is available, when compared to the registration of 2D images. As such, registration of 2D anatomical images may actually require that more resolution be spent for additional SNR to generate the sufficient contrast needed for optimal registration. However, the majority of registration processing pipelines are implemented to analyze 3D datasets, e.g., in the neuroimaging community for morphometry, and the results found in this investigation imply that imaging for given scan times can be optimized for these pipelines based on SNR.

It is not the intention of this study to direct readers to acquire images with an SNR of 20 for every task. Rather, for the specific task of registration in the context of anatomical images, this SNR should be the target when there are no other conflicting purposes. If data were acquired with SNR not equal to 20, for some other task, then, while registration would still likely converge to a solution, the solution would not likely be the optimal one attainable for the given scan time.

CONCLUSIONS

Image registration has matured into a powerful utility in medical imaging to the point where it is used as the fundamental tool in a variety of studies, such as anatomical phenotyping in MR data [Lee et al., 2007; Nieman et al., 2006]. In such cases, accuracy of registration is the vital component to an experiment, and imaging needs to be optimized for this computer-processing task. Here, the time-constrained tradeoff problem between SNR and resolution has been investigated for best registration accuracy.

For intensity-based registration methods employing affine and elastic deformations, we have shown that a tradeoff SNR of 20 for fixed imaging times provides the best images. Imaging situations, where acquisition time is limited and that use registration for morphometry via deformation fields, should adjust imaging parameters to achieve voxel SNRs of $\sim$20 for the most accurate registration.

ACKNOWLEDGMENTS

This work is a part of the Mouse Imaging Centre at the Hospital for Sick Children, with infrastructure funded by the Canada Foundation for Innovation and the Ontario Innovation Trust. The authors thank Victoria Bonn for specimen preparation, Nir Lifshitz and Jun Dazai for design/construction of the imaging probe, and Brian Nieman for pulse sequence development. Dr. R. Mark Henkelman holds a Canada Research Chair in Imaging, Jason Lerch is funded by a CIHR postdoctoral research fellowship, and Shoan Kale is a recipient of a NSERC graduate scholarship.

REFERENCES

Bajcsy R, Kovačič S (1989): Multiresolution elastic matching. Comput Vis Graph 46:1–21.

Bao P, Zhang L (2003): Noise reduction for magnetic resonance images via adaptive multiscale products thresholding. IEEE Trans Med Imaging 22:1089–1099.

Behin R, Bishop J, Henkelman RM (2005): Dynamic range requirements for MRI. Concepts Magn Reson 26B:28–35.

Christensen GE, Rabbitt RD, Miller MI (1996): Deformable templates using large deformation kinematics. IEEE Trans Image Process 5:1435–1447.

Collins DL, Evans AC (1997): ANIMAL: Validation and applications of nonlinear registration-based segmentation. Int J Pattern Recogn 11:1271–1294.

Collins DL, Neelin P, Peters TM, Evans AC (1994): Automatic 3D intersubject registration of MR volumetric data in standardized Talairach space. J Comput Assist Tomogr 18:192–205.

Collins DL, Holmes CJ, Peters TM, Evans AC (1995): Automatic 3D model-based neuroanatomical segmentation. Hum Brain Mapp 3:190–208.

Constable RT, Gore JC (1992): The loss of small objects in variable TE imaging: Implications for FSE, RARE, and EPI. Magn Reson Med 28:9–24.

Constable RT, Henkelman RM (1991): Contrast, resolution, and detectability in MR imaging. J Comput Assist Tomogr 15:297–303.

Crum WR, Griffin LD, Hill DLG, Hawkes DJ (2003): Zen and the art of medical image registration: Correspondence, homology, and quality. Neuroimage 20:1425–1437.

Edelstein WA, Glover GH, Hardy CJ, Redington RW (1986): The intrinsic signal-to-noise ratio in NMR imaging. Magn Reson Med 3:604–618.

Field DJ (1987): Relations between the statistics of natural images and the response properties of cortical-cells. J Opt Soc Am A 4:2379–2394.

Freeborough PA, Woods RP, Fox NC (1996): Accurate registration of serial 3D MR brain images and its application to visualizing change in neurodegenerative disorders. J Comput Assist Tomogr 20:1012–1022.

Friston KJ, Ashburner J, Frith CD, Poline J-B, Heather JD, Frackowiak RSJ (1995): Spatial registration and normalization of images. Hum Brain Mapp 3:165–189.

Fuderer M (1988): The information content of MR images. IEEE Trans Med Imaging 7:368–380.

Ghugre NR, Martin M, Scadeng M, Ruffins S, Hiltner T, Pautler R, Waters C, Readhead C, Jacobs R, Wood JC (2003): Superiority of 3D wavelet-packet denoising in MR microscopy. Magn Reson Imaging 21:913–921.

Henkelman RM (1985): Measurement of signal intensities in the presence of noise in MR images. Med Phys 12:232–233.

Henkelman RM, Dazai J, Lifshiftz N, Nieman BJ, Tsatskis S, Lerch JP, Bishop J, Kale S, Sled JG, Chen XJ (2006): High throughput microimaging of the mouse brain. Proc Int Soc Magn Reson Med (14) 2010.

Hill DLG, Hawkes DJ, Gleeson MJ, Cox TC, Strong AJ, Wong WL, Ruff CF, Kitchen ND, Thomas DG, Sofat A (1994): Accurate frameless registration of MR and CT images of the head: Applications in planning surgery and radiation therapy. Radiology 191:447–454.

Holden M, Hill DLG, Denton ERE, Jarosz JM, Cox TCS, Rohlfing T, Goodey J, Hawkes DJ (2000): Voxel similarity measures for 3-D serial MR brain image registration. IEEE Trans Med Imaging 19:94–102.

Holthoff VA, Beuthien-Baumann B, Kalbe E, Lüdecke S, Lenz O, Zündorf G, Spirling S, Schierz K, Winiecki P, Sorbi S, Herholz K (2005): Regional cerebral metabolism in early Alzheimer's disease with clinically significant apathy or depression. Biol Psychiatry 57:412–421.

Hyunjin P, Bland PH, Meyer CR (2003): Construction of an abdominal probabilistic atlas and its application in segmentation. IEEE Trans Med Imaging 22:483–492.

Kohn A (2002): Magnetic resonance imaging registration and quantitation of the brain before and after coronary artery bypass graft surgery. Ann Thorac Surg 73:S363–S365.

Kovacevic N, Henderson JT, Chan E, Lifshitz N, Bishop J, Evans AC, Henkelman RM, Chen XJ (2005): A three-dimensional MRI atlas of the mouse brain with estimates of the average and variability. Cereb Cortex 15:639–645.

Lee AD, Leow AD, Lu A, Reiss AL, Hall S, Chiang M, Toga AW, Thompson PM (2007): 3D pattern of brain abnormalities in Fragile X syndrome visualized using tensor-based morphometry. Neuroimage 34:924–938.

Lemieux L, Barker GJ (1998): Measurement of small inter-scan fluctuations in voxel dimensions in magnetic resonance images using registration. Med Phys 25:1049–1054.

Lerch JP, Tsatskis S, Sled JG, Kovacevic N, Henkelman RM (2006): Variability of automated shape analyses of fixed brain mouse MRI. Proc Int Soc Magn Reson Med (14) 1504.

Li B, Christensen GE, Hoffman EA, McLennan G, Reinhardt JM (2003): Establishing a normative atlas of the human lung. Acad Radiol 10:255–265.

Lu W, Olivera GH, Chen Q, Ruchala KJ, Haimerl J, Meeks SL, Langen KM, Kupelian PA (2006): Deformable registration of the planning image (kVCT) and the daily images (MVCT) for adaptive radiation therapy. Phys Med Biol 51:4357–4374.

Maintz JBA, Viergever MA (1998): A survey of medical image registration. Med Image Anal 2:1–36.

Mega MS, Lee L, Dinov ID, Mishkin F, Toga AW, Cummings JL (2000): Cerebral correlates of psychotic symptoms in Alzheimer's disease. J Neurol Neurosurg Psychiatry 69:167–171.

Miller MI (2004): Computational anatomy: Shape, growth, and atrophy comparison via diffeomorphisms. Neuroimage 23:S19–S33.

Narr KL, Toga AW, Szeszko P, Thompson PM, Woods RP, Robinson D, Sevy S, Wang Y, Schrock K, Bilder RM (2005): Cortical thinning in cingulate and occipital cortices in first episode Schizophrenia. Biol Psychiatry 58:32–40.

Nieman BJ, Flenniken AM, Adamson SL, Henkelman RM, Sled JG (2006): Anatomical phenotyping in the brain and skull of a mutant mouse by magnetic resonance imaging and computed tomography. Physiol Genomics 24:154–162.

Nishimura D (1996): Noise considerations. In: Principles of Magnetic Resonance Imaging. Palo Alto, CA: Stanford University Press. pp 158–168.

Owen RS, Wehrli FW (1990): Predictability of SNR and reader preference in clinical MR imaging. Magn Reson Imaging 8:737–745.

Puri BK, Hutton SB, Saeed N, Oatridge A, Hajnal JV, Duncan L, Chapman MJ, Barnes TRE, Bydder GM, Joyce EM (2001): A serial longitudinal quantitative MRI study of cerebral changes in first-episode Schizophrenia using image segmentation and subvoxel registration. Psychiatry Res 106:141–150.

Roeske JC, Forman JD, Mesina CF, He T, Pelizzari CA, Fontenla E, Vijayakumar S, Chen GTY (1995): Evaluation of changes in the size and location of the prostate, seminal vesicles, bladder, and rectum during a course of external beam radiation therapy. Int J Radiat Oncol 33:1321–1329.

Rüsch N, Tebartz van Elst L, Ludaescher P, Wilke M, Huppertz H-J, Thiel T, Schmahl C, Bohus M, Lieb K, Heßlinger B, Hennig J, Ebert D (2003): A voxel-based morphometric MRI study in female patients with borderline personality disorder. Neuroimage 20:385–392.

Sijbers J, den Dekker AJ, Scheunders P, Van Dyck D (1998): Maximum-likelihood estimation of Rician distribution parameters. IEEE Trans Med Imaging 17:357–361.

Sled JG, Zijdenbos AP, Evans AC (1998): A nonparametric method for automatic correction of intensity nonuniformity in MRI data. IEEE Trans Med Imaging 17:87–97.

Spring S, Lerch JP, Henkelman RM (2007): Sexual dimorphism revealed in the structure of the mouse brain using three-dimensional magnetic resonance imaging. Neuroimage 35: 1424–1433.

Thompson PM, Moussai J, Zohoori S, Goldkorn A, Khan AA, Mega MS, Small GW, Cummings JL, Toga AW (1998): Cortical variability and asymmetry in normal aging and Alzheimer's disease. Cereb Cortex 8:492–509.

Thompson PM, Mega MS, Woods RP, Zoumalan CI, Lindshield CJ, Blanton RE, Moussai J, Holmes CJ, Cummings JL, Toga AW (2001): Cortical change in Alzheimer's disease detected with a disease-specific population-based brain atlas. Cereb Cortex 11:1–16.

Toga AW, Thompson PM (2001): Maps of the brain. Anat Rec 265(B):37–53.

Tyszka JM, Readhead C, Bearer EL, Pautler RG, Jacobs RE (2006): Statistical diffusion tensor histology reveals regional dysmyelination effects in the shiverer mouse mutant. Neuroimage 29:1058–1065.

Zitová B, Flusser J (2003): Image registration methods: A survey. Image Vis Comput 21:977–1000.